ROYAL SOCIETY OF CHEMISTRY

PAPER

Check for updates

Electronic structure regulation of an ultra-thin MOF-derived NiSe$_2$/NiS$_2$@NC heterojunction for promoting the hydrogen evolution reaction†

Kebin Lu,‡[a] Jianpeng Sun,‡[a] Huakai Xu,[a] Chuanhai Jiang,[a] Weifeng Jiang,[a] Fangna Dai, [ID] *[a] Hong Wang*[b] and Hongguo Hao*[c]

Transition metal selenides (TMSes) are considered promising electrocatalysts for the hydrogen evolution reaction (HER) due to their narrow bandgap, unique morphology and low cost. Herein, using a metal–organic framework (MOF) as a precursor, a NiSe$_2$/NiS$_2$@NC electrocatalyst with abundant heterogeneous interfaces was designed and synthesized through a simultaneous selenization/sulfurization process. The heterojunction could provide more catalytic sites, accelerate the transfer of ions/gas, and optimize the electronic structure of the interface, and then exhibit overpotentials of 188 mV and 211 mV at 10 mA cm^{-2} in acidic and alkaline media. The density functional theory (DFT) calculation results showed that the heterogeneous interface can optimize the electronic structure. Meanwhile, the Gibbs free-energy for H* adsorption (ΔG_{H^*}) was reduced to −0.35 eV, which means that the interface can effectively accelerate the HER kinetics. This work provides a strategy for constructing heterojunction electrocatalysts and understanding the role of electronic structure in the HER.

Introduction

Hydrogen energy is an environmentally friendly, renewable, and high-energy-density new energy source, which has advantages in solving energy shortages and related environmental problems.[1–5] The electrochemical hydrogen evolution reaction (HER) is considered to be an efficient and sustainable hydrogen production method. However, to achieve high efficiency hydrogen production, it is necessary to overcome a certain potential energy barrier, which places high demands on the catalyst.[6–8]

Due to their narrow bandgap, unique morphology and low cost, transition metal selenides (TMSes) have been widely used as HER electrocatalysts in recent years.[9–12] However, their performances are limited by low conductivity and the lack of effective active sites. Therefore, improving the electrocatalytic performance of TMSes is still a big challenge.[13,14] The

construction of heterojunctions and idiographic nano-interfaces can control the electronic structure and optimize the chemical adsorption of reaction intermediates to accelerate the electrocatalytic kinetics.[15] In addition to metal doping,[16,17] non-metal doping is also considered to be another promising strategy to construct heterojunctions. For instance, Guo *et al.* anchored CoS$_2$ nanoparticles onto the surface of CoSe$_2$/DETA (diethylenetriamine) and constructed a CoS$_2$/CoSe$_2$ hybrid material, which not only exhibits excellent catalytic activity but also has good mechanical properties.[18] Wang *et al.* have synthesized a nickel foam-supported NiSe$_2$–Ni$_2$P heterojunction catalyst used in acidic solution, which improved the catalytic activity of the main catalyst through the coupling effect between NiSe$_2$ and Ni$_2$P.[19] The above work has made certain improvements and obtained a heterojunction catalyst with good catalytic activity, but an in-depth study on the specific influence of the heterogeneous interface is severely lacking. Thus, it is essential to carry out systematic experimental and theoretical research for constructing non-metal doped heterojunction TMSes and understand the regulation of the electronic structure of the catalyst.

Based on the above considerations, we chose a Ni-MOF ([Ni(HBTC)(DABCO)]) (HBTC = trimesic acid, DABCO = 1,4-diazabicyclo [2.2.2] octane) nanosheet as the precursor, and successfully synthesized a NiSe$_2$/NiS$_2$@NC (NC = nitrogen-doped carbon matrix) heterojunction electrocatalyst after high-temperature carbonization and simultaneous selenization/sulfurization. Choosing a

[a] College of Science, School of Materials Science and Engineering, China University of Petroleum (East China), Qingdao, Shandong, 266580, P. R. China. E-mail: fndai@upc.edu.cn
[b] A College of Materials Science and Engineering, Beijing University of Chemical Technology, Beijing, P. R. China. E-mail: wanghong@mail.buct.edu.cn
[c] Shandong Provincial Key Laboratory of Chemical Energy Storage and Novel Cell Technology, School of Chemistry and Chemical Engineering, Liaocheng University, Liaocheng 252059, China. E-mail: hhg207@126.com

suitable precursor can not only simplify the preparation process, but also facilitate the introduction of heteroatoms.[20–25] The MOF nanosheet as the preassembly platform is based on the following considerations:[26–28] first, the MOF nanosheet could generate more vacancies after pyrolysis, thereby increasing the number of catalytic sites; second, the nanosheet will crimp naturally during the calcination process to form a stable NC protective layer to avoid corrosion by the acid–base electrolyte; third, a small amount of carbon layer derived from the MOF nanosheet can prevent the agglomeration of metal sites.[29–35]

In the synthesized heterojunction, a rich phase interface is formed. Therefore, the hybrid material has low overpotentials of 188 mV and 211 mV at 10 mA cm^{-2} and shows promising stability in acidic and alkaline electrolytes. Density functional theory (DFT) calculations show that the multiphase interface can adjust the electronic structure of NiSe$_2$/NiS$_2$@NC, thereby changing the Gibbs free energy of hydrogen-containing intermediates. After the interface engineering control, the ΔG_{H^*} in the HER process decreases from -0.518 eV (NiSe$_2$@NC) and -1.11 eV (NiS$_2$@NC) to -0.35 eV (NiSe$_2$/NiS$_2$@NC). The combination of experimental and theoretical research proves that a distinctive two-phase interface is necessary to adjust the electronic structure and optimize the inherent HER performance of a TMSe electrocatalyst.

Experimental

Materials and methods

All the reagents were used as received without further purification. Nickel nitrate hexahydrate (Ni(NO$_3$)$_2$·6H$_2$O), *N*,*N*-dimethylmethanamide (DMF) and methanol (MeOH) were purchased from Sigma-Aldrich (USA). 1,4-Diazabicyclo [2.2.2] octane (DABCO), trimesic acid (H$_3$-BTC), and polyethylene pyrrolidone (PVP) were purchased from Energy-Chemicals. Selenium (Se) powder and sulfur (S) powder were purchased from Sinopharm Chemical Reagent Co. Ltd. The water used for experiments was deionized (DI) water.

Preparation of ultrathin MOF nanosheets

The MOF nanosheets ([Ni(HBTC)(DABCO)]) used in this work were synthesized by a solvothermal method. First, 0.145 g (0.5 mmol) Ni(NO$_3$)$_2$·6H$_2$O, 0.056 g (0.5 mmol) DABCO, 0.053 g (0.25 mmol) H$_3$-BTC and 1 g PVP were dissolved in DMF (10 mL) solution. Then the resulting mixed solution was stirred at room temperature for 30 minutes, and finally the mixed solution was transferred to a 25 ml reactor, heated to 120 °C and kept for 24 hours. After being gradually cooled to room temperature, collected by centrifugation and washed with DMF and methanol three times, the final ultrathin MOF nanosheets were obtained after drying at 80 °C for 12 hours under vacuum conditions.

Synthesis of Ni@NC

For the synthesis of Ni@NC nanomaterials, the MOF nanosheet was transferred to a square porcelain boat followed by placing it in a furnace. And the furnace was heated from room temperature to 600 °C for 2 hours with a heating rate of 5 °C min^{-1} under an argon atmosphere. The argon gas should flow for 30 minutes to ensure that the reaction is carried out in an argon atmosphere before heating.

Synthesis of NiSe$_2$@NC, NiS$_2$@NC, and NiSe$_2$/NiS$_2$@NC

20 mg Ni@NC and 120 mg selenium powder (sulfur powder, 60 mg sulfur powder, and 60 mg selenium powder) were accurately weighed and placed in a square ceramic boat, which was then placed in the furnace. In an argon atmosphere, the furnace was heated from room temperature to 450 °C for 2 hours, and the heating rate was 5 °C min^{-1}. The argon gas should flow for 30 minutes to ensure that the reaction is carried out in an argon atmosphere before heating.

Materials characterization

The phase of electrocatalysts was characterized through X-ray diffraction (XRD, Bruker D2 PHASER). The nitrogen adsorption–desorption isotherms were obtained using a Bel Japan BELSORP-MINIII. The morphologies were obtained using a scanning electron microscope (SEM, HITACHI S-8200) and a transmission electron microscope (TEM, Hitachi JEM-2100F). X-ray photoelectron spectroscopy (XPS) spectra were recorded using a Thermo Scientific ESCALAB 250Xi.

Electrochemical measurements

All HER tests in this article were performed with a typical three-electrode system (Gamry INTERFACE 1000 T) at room temperature. In the measurements, a three-electrode system was employed with a graphite carbon rod, a calomel electrode (SCE) and a glassy carbon electrode (GCE) as the counter electrode, reference electrode and working electrode, respectively. The details of the measurements are included in the ESI.†

Density functional theory (DFT) calculations

Density functional theory (DFT) calculations were performed using the Vienna *ab initio* Simulation Package (VASP) with the generalized gradient approximation (GGA) parameterized by Perdew, Burke and Ernzerhof (PBE) for the exchange correlation functional. The details of the calculations are included in the ESI.†

Results and discussion

The synthetic procedures of NiSe$_2$/NiS$_2$@NC are shown in Fig. 1a. The X-ray diffraction (XRD) pattern, FT-IR spectra (Fig. S1, ESI†) and Brunauer–Emmett–Teller (BET) measurements (Fig. S2, ESI†) of the MOF are consistent with the reported work,[36] which proves that it has a high phase purity. Moreover, from the thermo-gravimetric analysis (TGA) curve (Fig. S5a, ESI†), the MOF framework has collapsed after 400 °C. Therefore, 600 °C is chosen as the carbonization temperature. The atomic force microscopy (AFM) image (Fig. S3, ESI†) shows
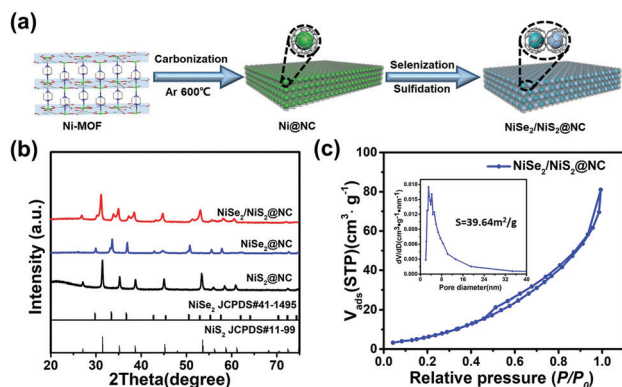
Fig. 1 (a) Schematic illustration of the two-step synthetic procedures of NiSe$_2$/NiS$_2$@NC. (b) XRD patterns. (c) N$_2$ adsorption–desorption isotherms (inset: pore size distribution curve).

Fig. 2 Raman spectra of (a and b) NiSe$_2$@NC, (c) NiS$_2$@NC, and (d) NiSe$_2$/NiS$_2$@NC.

the ultrathin MOF nanosheet with a thickness of 6 nm. From the structure diagram of the MOF (Fig. S4, ESI†), it can be considered that the number of MOF layers synthesized in this paper is 8 ± 1.

The Ni-MOF was transformed into Ni@NC through a two hour annealing step at 600 °C under an Ar atmosphere. The XRD peaks of Ni@NC (Fig. S6, ESI†) are consistent with the Ni@NC (JCPDS# 04-0850) standard pattern. Then, the NiSe$_2$/NiS$_2$@NC was prepared by simultaneously introducing S and Se in an Ar atmosphere at 450 °C. For comparison, NiSe$_2$@NC and NiS$_2$@NC were prepared by separately introducing selenium or sulfur. The XRD peaks of NiSe$_2$@NC and NiS$_2$@NC match well with NiSe$_2$ (JCPDS# 41-1495) and NiS$_2$ (JCPDS# 11-99) standard patterns (Fig. 1b). The XRD peaks of NiSe$_2$/NiS$_2$@NC show the combination of two types of peaks, which indicates the successful preparation of the NiSe$_2$/NiS$_2$@NC. NiSe$_2$/NiS$_2$@NC has a specific surface area of 39.64 m^2 g^{-1} and larger N$_2$ adsorption capacity (Fig. 1c) than NiS$_2$@NC (Fig. S7, ESI†) and NiSe$_2$@NC (Fig. S8, ESI†). Meanwhile, the inset in Fig. 1c also shows a mesoporous structure of 2–16 nm in NiSe$_2$/NiS$_2$@NC. Such a large pore size is sufficient to allow the generated hydrogen to pass through, thereby promoting the HER process and improving the catalytic activity of the catalyst.[37]

In order to further explore the composition of the synthesized material, the material was characterized by Raman spectroscopy. Fig. 2a and b show that the peaks at 205, 360, 516, and 1062 cm^{-1} can be labeled as nickel selenide according to previously reported articles.[38,39] The observed peak in Fig. 2c at 467 cm^{-1} is the characteristic peak of the NiS$_2$@NC crystal.[40] From Fig. 2d, the peaks belonging to NiSe$_2$@NC and NiS$_2$@NC can be found, which further proves the successful preparation of NiSe$_2$/NiS$_2$@NC. In addition, the G band and D band are respectively related to the degree of graphitization of amorphous carbon. The peaks corresponding to the G band and D band of graphene layers located at 1345 and 1579 cm^{-1} can be observed in every spectrum, respectively, implying the presence of C in the composite. It is meaningful that the peak intensity ratio (I_D/I_G) can reflect the degree of defects on the surface of carbon materials and the degree of graphitization.[41,42]
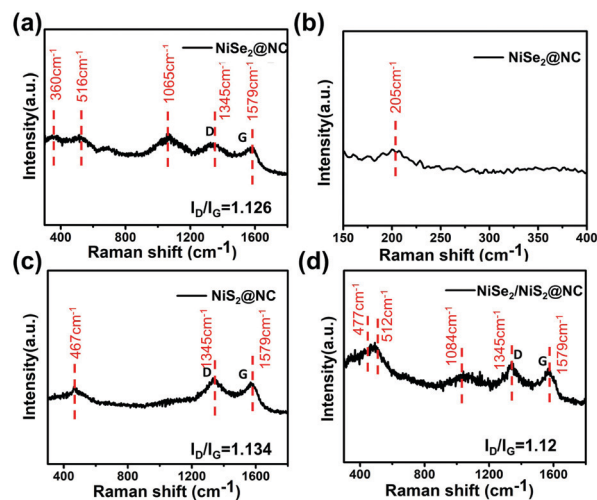
The peak intensity ratio of NiSe$_2$/NiS$_2$@NC is slightly smaller, which indicates that it has a higher degree of graphitization and better conductivity.

Transmission electron microscopy (TEM) can help us obtain the morphology of the sample, so TEM characterization of the material is carried out. During the calcination process of the Ni-MOF, Ni cations were reduced to Ni nanoparticles and organic ligands were pyrolyzed into N-doped graphene layers,[43] forming core–shell Ni@NC nanomaterials (Fig. 3b). The TEM image (Fig. 3c) of NiSe$_2$/NiS$_2$@NC also shows that NiSe$_2$/NiS$_2$ nanoparticles are wrapped in a thin N-doped graphene layer. The high-resolution transmission electron microscopy (HRTEM) image (Fig. 3d) shows two lattice fringes, namely NiS$_2$
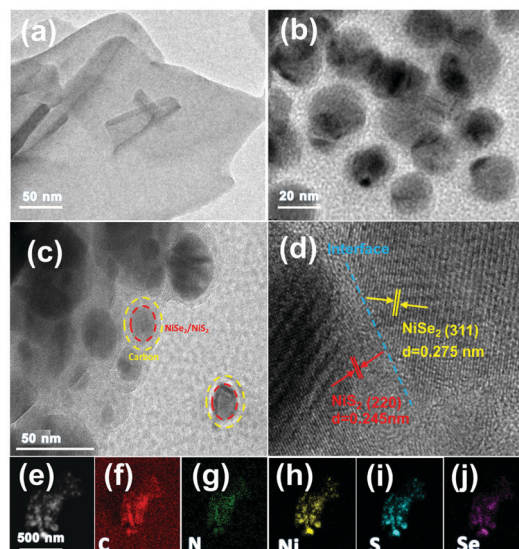

Fig. 3 (a) TEM image of the MOF. (b) TEM image of the Ni@NC. (c) TEM image of the NiSe$_2$/NiS$_2$@NC. (d) HRTEM image of the NiSe$_2$/NiS$_2$@NC. (e–j) EDS elemental mapping images showing C, N, Ni, S, and Se in the NiSe$_2$/NiS$_2$@NC.

(d = 0.245 nm) and NiSe$_2$ (d = 0.275 nm) lattice fringes, corresponding to the NiS$_2$ (220) facet and NiSe$_2$ (311) facet. The clear phase boundary between the NiS$_2$ and NiSe$_2$ crystals in Fig. 3d indicates that the heterogeneous interface has been successfully constructed.[44,45] The characteristic heterojunction can provide more active sites, and shorten the transport path of electrons. The mapping result shows the uniform distribution of C, N, Ni, S and Se elements in NiSe$_2$/NiS$_2$@NC in Fig. 3e–j.

In addition to the above characterization, this work also involved X-ray photoelectron spectroscopy (XPS). The XPS spectrum clearly reveals the main elements contained, including S, Se, Ni, C, N and O produced by inevitable oxidation (Fig. 4a).[46] The Ni 2p spectra (Fig. 4b) display the same shape as previously reported.[47] The two peaks at 854.1 eV and 870.8 eV prove the presence of Ni^{2+}. The peaks at 856.2 eV and 875.4 eV indicate the presence of Ni^{3+}, which can be attributed to the slight oxidation of the surface. The peaks near 860.5 eV and 880.6 eV are the satellites of Ni 2p$_{3/2}$ and Ni 2p$_{1/2}$, which are consistent with the results reported in the literature.[48] The S 2p spectrum can be fitted into two peaks at binding energies of 163.7 and 162.7 eV (Fig. 4c), corresponding to the S 2p$_{1/2}$ and S 2p$_{3/2}$ of Ni–S bonding.[49] In Fig. 4d, two peaks corresponding to Se 3d$_{5/2}$ (54.7 eV) and Se 3d$_{3/2}$ (55.8 eV) can be fitted, which proves the existence of the Se–Ni bond. And the peak at 59.1 eV is caused by the SeO$_x$ species due to the exposure to air.[50] In addition, the C 1s spectra (Fig. 4e) can also be fitted into two peaks at 284.6 and 285.3 eV, which are ascribed to the C–C and C–N/C–O species, respectively.[32] Based on the N 1s spectra (Fig. 4f), three peaks with binding energies of 398.6, 401.2 and 402.8 eV correspond to pyridinic-N, pyrrolic-N and graphitic-N, respectively. What's more, a peak at about 1.5 eV higher than pyridine-N binding energy was also found at 400.3 eV, which was classified as an M–N$_x$ bond in some previous reports.[51,52] Therefore, it can be considered that there is a strong Ni–N$_x$ chemical bond between NiSe$_2$/NiS$_2$ and NC. The Ni–N$_x$ bond not only greatly promotes the interface electron transfer, but also maximizes the synergistic effect induced.

In order to reveal the influence of the electronic structure of the heterogeneous interface on the electrocatalytic performance, a standard three-electrode system was used to evaluate
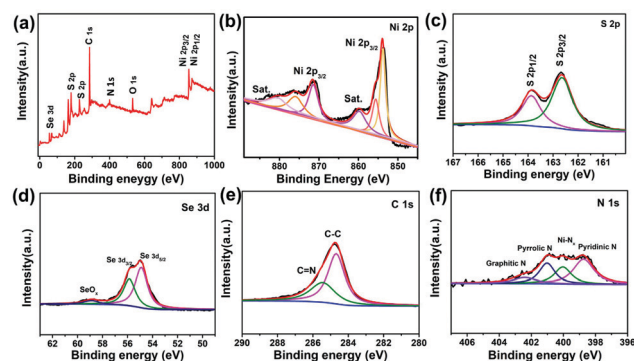

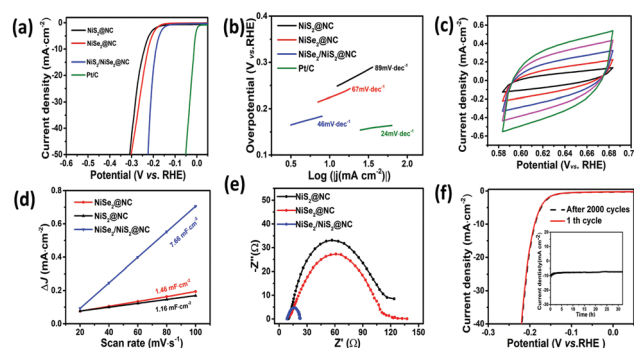Fig. 5 The HER performance in 0.5 M H$_2$SO$_4$ solution: (a) LSV curves; (b) Tafel plots; (c) the CV curves of NiSe$_2$/NiS$_2$@NC; (d) the electrochemical double-layer capacitance (C_{dl}); (e) EIS data; (f) LSV curves of NiSe$_2$/NiS$_2$@NC before and after 2000 cycles for stability test. (Inset: time dependent current density (i–t) curves of NiSe$_2$/NiS$_2$@NC.)

the HER activity in 0.5 M H$_2$SO$_4$ solution. First, NiSe$_2$/NiS$_2$@NC was synthesized at synthesis temperatures of 350 °C, 450 °C, and 550 °C, respectively, and the optimum synthesis temperature was investigated. The results manifest that when the synthesis temperature is 450 °C, the overpotential to reach −10 mA cm^{-2} is the smallest (Fig. S10, ESI†). What's more, for comparison, 20% Pt/C, NiSe$_2$@NC and NiS$_2$@NC were also evaluated. As expected, 20% Pt/C exhibited the best catalytic properties, and the HER activity of NiSe$_2$/NiS$_2$@NC (188 mV) was also better than those of NiSe$_2$@NC (244 mV) and NiS$_2$@NC (240 mV) (Fig. 5a).

The Tafel diagram derived from the polarization curve can help in further studying the reaction kinetics of the catalyst. When the current density increases, a smaller Tafel slope means higher HER efficiency. At the same time, the reaction mechanism of the HER in acidic electrolytes is divided into two main steps according to the Tafel diagram:[53–55] Volmer (120 mV dec^{-1}), Heyrovsky (40 mV dec^{-1}) or Tafel (30 mV dec^{-1}) steps. As seen in Fig. 5b, the Tafel slope of NiSe$_2$/NiS$_2$@NC (46 mV dec^{-1}) is lower than those of NiSe$_2$@NC (67 mV dec^{-1}) and NiS$_2$@NC (89 mV dec^{-1}), indicating that NiSe$_2$/NiS$_2$@NC has higher HER efficiency, and the HER process should belong to the Volmer–Heyrovsky mechanism.

Besides the intrinsic activity of the catalyst, the HER catalytic performance of the material is also closely related to the actual electrochemical active surface area (ECSA). In the non-Faraday response region, the ECSA of the material can be estimated using the double-layer capacitance (C_{dl}). Therefore, we have explored the ECSA of NiSe$_2$/NiS$_2$@NC on the basis of the corresponding electrochemical C_{dl}. The C_{dl} values of the three materials can be calculated through the CV curves (Fig. S11 and Fig. 5c, ESI†). It can be seen from Fig. 5d that NiSe$_2$/NiS$_2$@NC has the highest C_{dl} value, which shows that its ECSA value is higher. After that, electrochemical impedance spectroscopy (EIS) was used to determine the electrode kinetics of NiSe$_2$/NiS$_2$@NC. As shown in Fig. 5e, NiSe$_2$/NiS$_2$@NC has the lowest charge transfer resistance, which makes the electron transfer speed in the HER faster. In addition, the stability of the catalyst
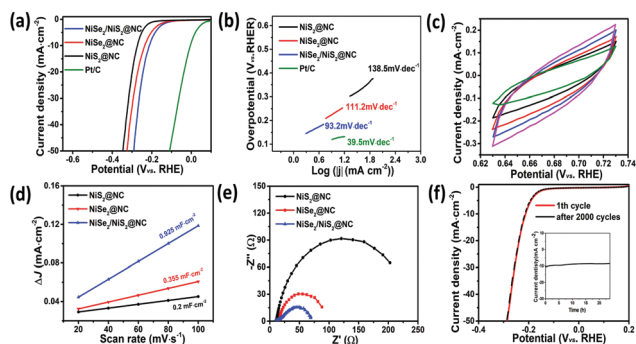

Fig. 4 XPS spectra of NiSe$_2$/NiS$_2$@NC: (a) XPS spectra, (b) Ni 2p, (c) S 2p, (d) Se 3d, (e) C 1s, and (f) N 1s.

Fig. 6 The HER performance in 1.0 M KOH solution: (a) LSV curves; (b) Tafel plots; (c) the CV curves of NiSe$_2$/NiS$_2$@NC; (d) the C_{dl}; (e) EIS data; (f) LSV curves of NiSe$_2$/NiS$_2$@NC before and after 2000 cycles of the stability test. (Inset: time dependent current density (i−t) curves of NiSe$_2$/NiS$_2$@NC).

Fig. 7 (a) The theoretical models of NiSe$_2$/NiS$_2$@NC used in the DFT calculations. (b) Differential charge density between NiS$_2$@NC and NiSe$_2$@NC. (c) The projected electronic density of states (PDOS) of NiSe$_2$/NiS$_2$@NC. (d) Gibbs free-energy diagram for H* adsorption (ΔG_{H*}).

is of great significance to its subsequent practical applications, for which we researched the electrochemical stability of NiSe$_2$/NiS$_2$@NC. The initial overpotential and current density did not change much after 2000 continuous CV cycles, as seen from the LSV curves (Fig. 5f). Meanwhile, in the stability test for 32 h, NiSe$_2$/NiS$_2$@NC also showed excellent stability.

In addition, the catalytic effect of the catalyst in 1.0 M KOH solution was also explored (Fig. 6). NiSe$_2$/NiS$_2$@NC only requires 211 mV of overpotential at −10 mA cm^{-2}, which is lower than those of NiSe$_2$@NC (236 mV) and NiS$_2$@NC (272 mV). In addition, the Tafel slope of NiSe$_2$/NiS$_2$@NC is also smaller, indicating that it has a higher HER efficiency. Simultaneously, the Tafel slope of 93.2 mV dec^{-1} indicates that the HER process should belong to the Volmer–Heyrovsky mechanism under alkaline conditions. The C_{dl} value of NiSe$_2$/NiS$_2$@NC is higher, which shows that it has a larger active area. Moreover, the charge transfer resistance of NiSe$_2$/NiS$_2$@NC is much smaller, which is more conducive to the progress of the HER. The cycling performance and long-term stability were verified using the polarization curve (1st and 2000th) and constant 24 h stability test. Besides, the HER performance of NiSe$_2$/NiS$_2$@NC was also investigated in neutral medium. According to the LSV curve, NiSe$_2$/NiS$_2$@NC shows a comparatively lower onset potential and overpotential at −10 mA cm^{-2} than those in acidic and alkaline media, owing to its sluggish reaction barriers under this condition. The corresponding Tafel slope is also calculated and is presented in Fig. S18 (ESI†).

After the electrocatalytic activity tests under acidic and alkaline conditions, the synthesized NiSe$_2$/NiS$_2$@NC heterojunction shows the expected HER electrocatalytic activity, which exceeds those of many reported materials (Tables S1 and S2, ESI†). In order to have a deeper understanding of the influence of the NiSe$_2$/NiS$_2$@NC heterojunction on the electrocatalytic performance, we conducted DFT calculations under acidic conditions and studied the interface charge behavior.

In order to analyze the differential charge density, a model of the NiSe$_2$/NiS$_2$@NC crystal structure as shown in Fig. 7a was constructed. The differential charge density shows that the
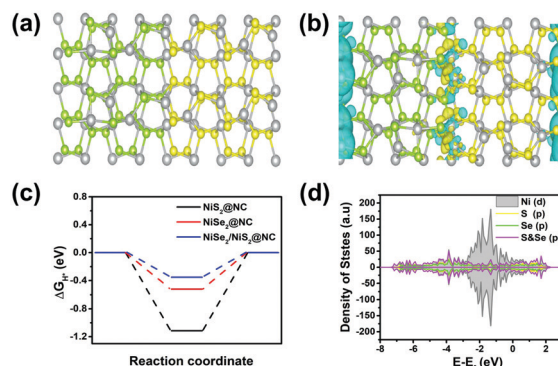
electron density increases significantly near the two-phase interface (Fig. 7b), indicating the accumulation of electrons near the interface. In addition, the ΔG_{H*} on the catalyst surface is generally considered to be one of the keys to evaluating the activity of the catalyst. It is generally believed that the closer the absolute value of ΔG_{H*} is to zero, the better the electrocatalytic activity. Therefore, we performed DFT calculations on the ΔG_{H*} value. To simplify the calculation process, we have established a model of H atom adsorption on the surfaces of NiSe$_2$, NiS$_2$, and NiSe$_2$/NiS$_2$ (Fig. S13–S15, ESI†). The ΔG_{H*} values of NiSe$_2$@NC, NiS$_2$@NC, and NiS$_2$/NiS$_2$@NC in Fig. 7c are approximately −0.518 eV, −1.11 eV and −0.35 eV. At the same time, the ΔG_{H*} value of NiSe$_2$/NiS$_2$@NC is smaller than the ΔG_{H*} values of NiSe$_2$@NC (0.565 eV)[56] and NiS$_2$@NC (−1.2 eV)[57] reported in the literature. The decrease of the ΔG_{H*} value indicates that NiSe$_2$/NiS$_2$@NC not only has the lowest hydrogen adsorption energy, but also accelerates the proton/electron transport, thereby improving the intrinsic catalytic activity.[58]

To further explore its origin, the projected electronic density of states (PDOS) calculations are performed for NiSe$_2$/NiS$_2$@NC (Fig. 7d), respectively. Ni 3d band and the S/Se p band centers were obtained by integrating the PDOS. The smaller difference between the Ni 3d and Se/S p band centers indicates a lower charge transfer energy, indicating that the covalency between Ni and Se/S is stronger.[59] It is worth noting that due to the moderate covalent properties, the interaction between the hydrogen containing intermediate and the Ni site is relatively suitable on NiSe$_2$/NiS$_2$@NC, indicating that the heterogeneous interface promotes the HER process to a certain extent.

Conclusions

In short, a Ni-MOF is used as the precursor to synthesize a NiSe$_2$/NiS$_2$@NC heterojunction with rich phase interfaces through the process of first carbonization and then simultaneous selenization/sulfurization. The heterojunction has more catalytic sites, and can accelerate the transfer of ions/gas, and

regulate the electronic structure of the interface. In addition, the catalyst exhibits overpotentials of 188 mV and 211 mV at 10 mA cm^{-2} in acidic and alkaline media. Moreover, the DFT calculations show that the electron transfer at the heterogeneous interface can adjust the electronic structure of NiSe$_2$/NiS$_2$@NC and further change the ΔG_{H^*}. This work provides an inimitable strategy for exploring the construction of heterojunction electrocatalysts for the HER using MOFs as a template.

Author contributions

Kebing Lu and Jianpeng Sun: contributed equally to conceptualization, methodology, investigation, and writing – original draft. Weifeng Jiang, Chuanhai Jiang, and Huakai Xu: validation and writing – review & editing. Fangna Dai, Hong Wang and Hongguo Hao: resources, supervision, project administration, and funding acquisition.

Conflicts of interest

There are no conflicts to declare.

Acknowledgements

Notes and references

1 S. Kang, J. Bang, K. Chung, C. Nandadasa, G. Han, S. Lee, K. Lee, K. Lee, Y. Ma, S. Oh, S. Kim, Y. Kim and S. Kim, *Sci. Adv.*, 2020, **6**, eaba7416.
2 A. Baroutaji, T. Wilberforce, M. Ramadan and A. G. Olabi, *Renewable Sustainable Energy Rev*, 2019, **106**, 31–40.
3 X. Zou and Y. Zhang, *Chem. Soc. Rev.*, 2015, **44**, 5148–5180.
4 A. Dhakshinamoorthy, Z. Li and H. Garcia, *Chem. Soc. Rev.*, 2018, **47**, 8134–8172.
5 H. Ang, H. Wang, B. Li, Y. Zong, X. Wang and Q. Yan, *Small*, 2016, **12**, 2859.
6 A. Indra, T. Song and U. Paik, *Adv. Mater.*, 2018, **30**, 1705146.
7 X. Wang, B. Zheng, B. Yu, B. Wang, W. Hou, W. Zhang and Y. Chen, *J. Mater. Chem. A*, 2018, **6**, 7842–7850.
8 J. Ekspong, T. Sharifi, A. Shchukarev, A. Klechikov, T. Wågberg and E. Gracia-Espino, *Adv. Funct. Mater.*, 2016, **26**, 6766–6776.
9 T. Jaramillo, K. Jorgensen, J. Bonde, J. Nielsen, S. Horch and I. Chorkendorff, *Science*, 2007, **317**, 100–102.
10 S. Anantharaj, S. Rao Ede, K. Sakthikumar, K. Karthick, S. Mishra and S. Kundu, *ACS Catal.*, 2016, **6**, 8069–8097.
11 Z. Zheng, L. Yu, M. Gao, X. Chen, W. Zhou, C. Ma, L. Wu, J. Zhu, X. Meng, J. Hu, Y. Tu, S. Wu, J. Mao, Z. Tian and D. Deng, *Nat. Commun.*, 2020, **11**, 3315.
12 K. Zhou, J. He, X. Wang, J. Lin, Y. Jing, W. Zhang and Y. Chen, *Electrochim. Acta*, 2017, **231**, 626–631.
13 Y. Zhou, Y. Chen, M. Wei, H. Fan, X. Liu, Q. Liu, Y. Liu, J. Cao and L. Yang, *CrystEngComm*, 2021, **23**, 69.
14 K. Ao, J. Dong, C. Fan, D. Wang, Y. Cai, D. Li, F. Huang and Q. Wei, *ACS Sustainable Chem. Eng.*, 2018, **6**, 10952–10959.
15 Y. Li, Z. Yin, M. Cui, X. Liu, J. Xiong, S. Chen and T. Ma, *J. Mater. Chem. A*, 2021, **9**, 2070.
16 Y. Guan, Y. Feng, Y. Mu, H. Zhang and Y. Wang, *Electrochim. Acta*, 2017, **247**, 435–442.
17 G. Zhao, K. Rui, S. Dou and W. Sun, *Adv. Funct. Mater.*, 2018, **28**, 1803291.
18 Y. Guo, C. Shang and E. Wang, *J. Mater. Chem. A*, 2017, **5**, 2504.
19 P. Wang, Z. Pu, W. Li, J. Zhu, C. Zhang, Y. Zhao and S. Mu, *J. Catal.*, 2019, **377**, 600–608.
20 N. Li, Y. Zhang, M. Jia, X. Lv, X. Li, R. Li, X. Ding, Y.-Z. Zheng and X. Tao, *Electrochim. Acta*, 2019, **326**, 134976.
21 N. Chen, Q. Mo, L. He, X. Huang, L. Yang, J. Zeng and Q. Gao, *Electrochim. Acta*, 2019, **299**, 708–716.
22 X. Zhong, J. Tang, J. Wang, M. Shao, J. Chai, S. Wang, M. Yang, Y. Yang, N. Wang, S. Wang, B. Xu and H. Pan, *Electrochim. Acta*, 2018, **269**, 55–61.
23 X. Chen, Z. Qiao, B. Hou, H. Jiang, W. Gong, J. Dong, H.-Y. Li, Y. Cui and Y. Liu, *Nano Res.*, 2021, **14**, 466–472.
24 F. Dai, X. Wang, Y. Wang, Z. Liu and D. Sun, *Angew. Chem., Int. Ed.*, 2020, **5992**, 22372–22377.
25 Y.-B. Huang, J. Liang, X.-S. Wang and R. Cao, *Chem. Soc. Rev.*, 2017, **46**, 126.
26 L. Huang, G. Gao, H. Zhang, J. Chen, Y. Fang and S. Dong, *Nano Energy*, 2020, **68**, 104296.
27 X. Lu, Y. Fang, D. Luan and X. Lou, *Nano Lett.*, 2021, **21**, 1555.
28 Z. Huang, C. Feng, J. Sun, B. Xu, T. Huang, X. Wang, F. Dai and D. Sun, *CCS Chem.*, 2020, **2**, 2696–2711.
29 Y. Wang, Y. Pan, L. Zhu, H. Yu, B. Duan, R. Wang, Z. Zhang and S. Qiu, *Carbon*, 2019, **146**, 671–679.
30 H.-F. Wang, L. Pang, S. Kaskel and Q. Xu, *Chem. Soc. Rev.*, 2020, **49**, 1414.
31 B. Zhang, Y. Zheng, T. Ma, C. Yang, Y. Peng, Z. Zhou, M. Zhou, S. Li, Y. Wang and C. Cheng, *Adv. Mater.*, 2021, 2006042.
32 T. Wang, X. Cao and L. Jiao, *Small*, 2021, 2004398.
33 W. Zhou, J. Lu, K. Zhou, L. Yang, Y. Ke, Z. Tang and S. Chen, *Nano Energy*, 2016, **28**, 143–150.
34 X. Wu, S. Han, D. He, C. Yu, C. Lei, W. Liu, G. Zheng, X. Zhang and L. Lei, *ACS Sustainable Chem. Eng.*, 2018, **6**, 8672–8678.
35 J. Deng, J. Ren, D. Deng and X. Bao, *Angew. Chem., Int. Ed.*, 2015, **127**, 2128–2132.
36 S. Jeong, D. Kim, X. Song, M. Choi, N. Park and M. Lah, *Chem. Mater.*, 2013, **25**, 1047–1054.
37 F.-X. Ma, C.-Y. Xu, F. Lyu, B. Song, S.-C. Sun, Y. Li, J. Lu and L. Zhen, *Adv. Sci.*, 2019, **6**, 1801490.

38 W. Li, B. Yu, Y. Hu, X. Wang, D. Yang and Y. Chen, *ACS Sustainable Chem. Eng.*, 2019, **7**, 4351–4359.

39 P. Thangasamy, V. Maruthapandian, V. Saraswathy and M. Sathish, *Catal. Sci. Technol.*, 2017, **7**, 3591–3597.

40 D. W. Bishop, P.-S. Thomas and A. S. Ray, *Mater. Res. Bull.*, 2000, **35**, 1123–1128.

41 B. Wang, Z. Wang, X. Wang, B. Zheng, W. Zhang and Y. Chen, *J. Mater. Chem. A*, 2018, **6**, 12701–12707.

42 J. Lin, J. He, Y. Chen, Q. Li, B. Yu, C. Xu and W. Zhang, *Electrochim. Acta*, 2016, **215**, 667–673.

43 Y. Xu, W. Tu, B. Zhang, S. Yin, Y. Huang, M. Kraft and R. Xu, *Adv. Mater.*, 2017, **29**, 1605957.

44 Y. Yang, Y. Kang, H. Zhao, X. Dai, M. Cui, X. Luan, X. Zhang, F. Nie, Z. Ren and W. Song, *Small*, 2020, **16**, 1905083.

45 Z. Xue, X. Li, Q. Liu, M. Cai, K. Liu, M. Liu, Z. Ke, X. Liu and G. Li, *Adv. Mater.*, 2019, **31**, 1900430.

46 L. Yang, W. Hong, Y. Zhang, Y. Tian, X. Gao, Y. Zhu, G. Zou, H. Hou and X. Ji, *Adv. Funct. Mater.*, 2019, **29**, 1903454.

47 Y. Guo, D. Guo, F. Ye, K. Wang and Z. Shi, *Int. J. Hydrogen Energy*, 2017, **42**, 17038–17048.

48 P. Prieto, V. Nistor, K. Nouneh, M. Oyama, M. Abd-Lefdil and R. Díaz, *Appl. Surf. Sci.*, 2012, **258**, 8807–8813.

49 Y. Liang, Y. Yang, K. Xu, T. Yu, S. Yao, Q. Peng and C. Yuan, *J. Catal.*, 2020, **381**, 63–69.

50 J. Zhang, B. Jiang, J. Zhang, R. Li, N. Zhang, R. Liu, J. Li, D. Zhang and R. Zhang, *Mater. Lett.*, 2019, **235**, 53–56.

51 S.-L. Yang, T.-R. Zhang, G.-C. Li, L.-Q. Yang and J.-Y. Lee, *Energy Storage Mater.*, 2017, **6**, 140–148.

52 H. Zhang, Y. Liu, T. Chen, J. Zhang, J. Zhang and X. Lou, *Adv. Mater.*, 2019, **48**, 1904548.

53 Y.-H. Fang and Z.-P. Liu, *ACS Catal.*, 2014, **4**, 4364–4376.

54 X. Lu, S. Zhang, W. Sim, S. Gao and X. Lou, *Angew. Chem., Int. Ed.*, 2021, **60**, 22885.

55 M.-R. Gao, J.-X. Liang, Y.-R. Zheng, Y.-F. Xu, J. Jiang, Q. Gao, J. Li and S.-H. Yu, *Nat. Commun.*, 2015, **6**, 5982.

56 J. Lin, H. Wang, J. Cao, F. He, J. Feng and J. Qi, *J. Colloid Interface Sci.*, 2020, **571**, 260–266.

57 T. Wang, X. Guo, J. Zhang, W. Xiao, P. Xi, S. Peng and D. Gao, *J. Mater. Chem. A*, 2019, **7**, 4971.

58 X. Lv, W. Wei, H. Wang, B. Huang and Y. Dai, *Appl. Catal., B*, 2019, **255**, 117743.

59 W. Hong, K. Stoerzinger, Y. L. Lee, L. Giordano, A. Grimaud, A. Johnson, J. Hwang, E. Crumlin, W. Yang and S. Yang, *Energy Environ. Sci.*, 2017, **10**, 2190.